JOURNAL OF SYNCHROTRON RADIATION

ISSN: 1600-5775
journals.iucr.org/s

High-accuracy mass attenuation coefficients and X-ray absorption spectroscopy of zinc – the first X-ray Extended Range Technique-like experiment in Australia

Ruwini S. K. Ekanayake, Christopher T. Chantler, Daniel Sier, Martin J. Schalken, Alexis J. Illig, Martin D. de Jonge, Bernt Johannessen, Peter Kappen and Chanh Q. Tran

J. Synchrotron Rad. (2021). **28**, 1476–1491

JOURNAL OF SYNCHROTRON RADIATION

ISSN 1600-5775

Received 19 October 2020
Accepted 8 June 2021

Edited by R. W. Strange, University of Essex, United Kingdom

Keywords: materials science; XAFS; computational modelling; materials modelling; nanostructure; X-ray mass attenuation coefficients; XERT; X-ray absorption fine structure; integrated column density.

High-accuracy mass attenuation coefficients and X-ray absorption spectroscopy of zinc – the first X-ray Extended Range Technique-like experiment in Australia

Ruwini S. K. Ekanayake,[a] Christopher T. Chantler,[a]* Daniel Sier,[a] Martin J. Schalken,[a] Alexis J. Illig,[a] Martin D. de Jonge,[b] Bernt Johannessen,[b] Peter Kappen[b] and Chanh Q. Tran[c]

[a]School of Physics, University of Melbourne, Australia, [b]ANSTO, Australian Synchrotron, Melbourne, Australia, and [c]La Trobe University, Australia. *Correspondence e-mail: chantler@unimelb.edu.au

The first X-ray Extended Range Technique (XERT)-like experiment at the Australian Synchrotron, Australia, is presented. In this experiment X-ray mass attenuation coefficients are measured across an energy range including the zinc *K*-absorption edge and X-ray absorption fine structure (XAFS). These high-accuracy measurements are recorded at 496 energies from 8.51 keV to 11.59 keV. The XERT protocol dictates that systematic errors due to dark current nonlinearities, correction for blank measurements, full-foil mapping to characterize the absolute value of attenuation, scattering, harmonics and roughness are measured over an extended range of experimental parameter space. This results in data for better analysis, culminating in measurement of mass attenuation coefficients across the zinc *K*-edge to 0.023–0.036% accuracy. Dark current corrections are energy- and structure-dependent and the magnitude of correction reached 57% for thicker samples but was still large and significant for thin samples. Blank measurements scaled thin foil attenuation coefficients by 60–500%; and up to 90% even for thicker foils. Full-foil mapping and characterization corrected discrepancies between foils of up to 20%, rendering the possibility of absolute measurements of attenuation. Fluorescence scattering was also a major correction. Harmonics, roughness and bandwidth were explored. The energy was calibrated using standard reference foils. These results represent the most extensive and accurate measurements of zinc which enable investigations of discrepancies between current theory and experiments. This work was almost fully automated from this first experiment at the Australian Synchrotron, greatly increasing the possibility for large-scale studies using XERT.

1. Introduction

X-ray attenuation coefficients are a measure of how X-rays interact with matter and atoms and are widely used in many fields and techniques amongst the scientific community. Accurate experimental measurements of mass attenuation coefficients are important, as they provide many details about the local structure and local order and also interrogate current atomic and solid state quantum theoretical approaches. Mass attenuation coefficients have had notable limitations of accuracy caused by heterogeneity of the synchrotron flux and of the samples, in addition to the limitations of error analysis (Parratt *et al.*, 1959; Creagh, 1976; Creagh & Hubbell, 1999). This had been addressed by recognizing and correcting systematic errors, developing improved technologies by key X-ray absorption spectrometry (XAS) experiments (de Jonge *et al.*, 2004*a*, 2007; Tran *et al.*, 2005). Amongst these approa-

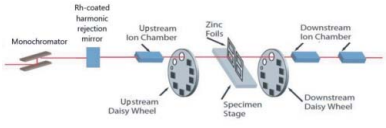

ches, the extended range measurement technique (XERT) is a prominent methodology of acquiring high-accuracy XAS with careful uncertainty analysis, for obtaining precise values of mass attenuation coefficients, and includes development of the synchrotron environment, the data collection procedure and data analysis. This approach has produced the most precise mass attenuation and XAFS measurements (de Jonge *et al.*, 2006, 2007; Chantler, 2009; Rae *et al.*, 2010*a*). The basic precept of XERT is to measure over an extended range of experimental parameter space, which allows recognition and quantification of key systematic effects that significantly affect the measurement, structure and accuracy of XAS and X-ray fluorescence.

XERT can evaluate reliable data on crystal structures, chemical bonding, thermal effects and fluorescence yields. The accuracy of XAFS measurements using XERT can be better than 0.05% (Chantler *et al.*, 2012*b*). Characteristic examples of measuring systematic errors include those of scattering and fluorescence effects (Chantler *et al.*, 2001*b*; Tran *et al.*, 2004*b*; Rae *et al.*, 2010*a*), higher harmonics of the beam from the monochromator (Tran *et al.*, 2003; Glover & Chantler, 2009), the bandwidth of the X-ray beam (de Jonge *et al.*, 2004*b*), sample roughness (Glover *et al.*, 2009; Tantau *et al.*, 2015), energy calibration (Rae *et al.*, 2010*c*; Glover *et al.*, 2010) and thickness calibration and normalization (Rae *et al.*, 2010*a*,*b*; Islam *et al.*, 2010). The mass attenuation coefficients of zinc metal have been derived by various techniques over wide ranges of energies. However, the quality of many measurements are questionable as they were determined without estimates of uncertainties (Ménesguen *et al.*, 2016). There are few reported previous measurements with uncertainties in the range 0.2–2%.

The National Institute of Standard and Technology (NIST) recommends two theoretical tabulations of the mass attenuation coefficients of elemental materials over large energy ranges: *XCOM* (Berger & Hubbell, 1987) and *FFAST* (Chantler, 1995, 2000). These tabulations have been critically tested with numerous high-accuracy experimental measurements. The *XCOM* program generates a comprehensive database of photon cross sections, photoelectric absorption and pair production and total attenuation coefficients for all elements or compounds with Hartree–Slater non-relativistic wavefunctions including Scofield relativistic perturbations over a wide range of energies ranging from 1 keV to 100 GeV. The *FFAST* approach computes real and imaginary components of form factors, photoelectric absorption and attenuation coefficients together with scattering contributions of elements within a self-consistent Dirac–Hartree–Fock framework.

Figure 1 represents the percentage differences between the mass attenuation coefficients obtained from various methods from the theoretically tabulated values using *FFAST*. The work of Hopkins (1959) is at variance with other data, and Unonius & Suorttri (1989) have few data points in this energy range. Theoretical tabulations using *XCOM* and the work of Henke & Shimabukuro (1982) have about 5% deviations from the *FFAST* tabulated data.

The mass attenuation coefficient of materials like zinc are important parameters for nuclear techniques such as computed tomography (CT) and gamma-ray attenuation analysis in agricultural areas to explore physical properties of soil (Borges *et al.*, 2014). Accurate values of mass attenuation coefficients are essential to yield better resolution in imaging applications especially in the medical field (Al-Buriahi & Tonguc, 2020; Huang & Wu, 1976). Zinc absorption spectra are used to identify the interaction level of zinc in many applications including estimates of dietary zinc absorption and natural food, the effect of human brain and body, and pregnancy associated conditions (Kaur *et al.*, 2014).

The most accurate claimed measurements of mass attenuation coefficients of zinc were made by Rae *et al.* (2010*a*) over an energy range 7.51–15.2 keV (black dots with error bars in Fig. 1). The uncertainties in the experimental measurements were obtained using XERT by quantifying the systematic errors. However, in that experiment the energy step and spacing were not optimized for XAFS measurements. Reported experimental references are inconsistent and do not agree with the theoretically calculated values. The values have a spread of about 15–30%. This large spread is unable to differentiate between the theoretical approaches.

This work determines the mass attenuation coefficients of zinc in the energy region 8.51–11.5914 keV including the zinc *K*-shell absorption edge (9.66076 keV) and the XAFS region. Experimental measurements were corrected for systematic errors including dark current, blank normalization, harmonics, energy offset, scattering and fluorescence. The local area

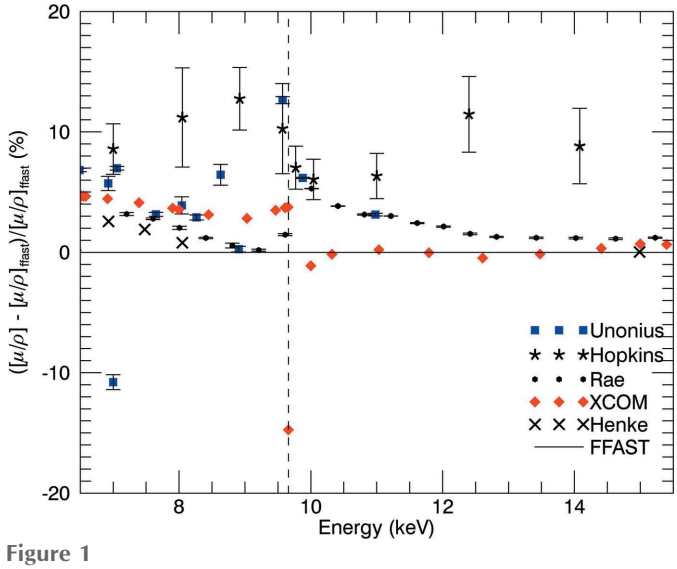

Figure 1
Experimental and theoretical values of mass attenuation coefficients of zinc. The percentage difference from the *FFAST* tabulated values of mass attenuation coefficients (Chantler, 1995, 2000) are plotted against energy. The dashed line indicates the energy of the absorption edge of zinc. Experimental results (Hopkins, 1959; Unonius & Suortti, 1989; Rae *et al.*, 2010*a*) are plotted with error bars. *XCOM* (Berger & Hubbell, 1987) tabulated theoretical values and Henke *et al.* (1982) interpreted values are also plotted, with no uncertainties reported. The discrepancy of experimental measurements exceeds the claimed accuracies. Few values are available near or above the edge. Rae *et al.* (2010*a*) deviates from the tabulated *FFAST* and *XCOM* values by 2% at 12 keV.

density of the foil is calibrated by calculating the absolute thickness using the full-foil mapping technique (de Jonge *et al.*, 2004*a*; Rae *et al.*, 2010*b*). This paper demonstrates the measurement of X-ray mass attenuation coefficients of zinc to a high accuracy. This high-accuracy data permit direct access to critical measurements of electron inelastic mean free paths (IMFP) and other key parameters.

This is the first XERT-like experiment in Australia. Previously XERT has been set up and implemented in Japan at the ANBF, at Chicago, and an initial foray at SSLC. Bringing the XERT formalism from ANBF back to Australia has involved developing and installing new hardware, recoding all software and control into new languages, and implementing new process variables. Interestingly, this is not so daunting as it might sound, but has of course required coordinated effort by beamline scientists and research groups. The location of this new high-precision high-accuracy tool permanently on a synchrotron beamline gives the prospect of uncovering information which is lost in conventional XAFS experiments. The proximity of the Australian Synchrotron has enabled a degree of automation that is not generally feasible under the 'suitcase science' paradigm. In this experiment, control routines were scripted up and launched once and only once; the entire body of measurements was able to be acquired in a fully automated fashion.

2. Experimental

XAS of zinc foils at room temperature were obtained at the XAS beamline ID12 at the Australian Synchrotron using an XERT-like experimental setup (Fig. 2). The X-ray beam was produced by a 1.9 T wiggler source. A Si(111) double-reflection crystal monochromator (DCM) was used to define the photon energy and predicts a bandwidth of about $\Delta E/E \simeq 1.5 \times 10^{-4}$. The DCM was operated at the peak of the rocking curve ('fully tuned'). To manage harmonics, two mirrors (Rh-coated) were used. The first mirror, upstream from the DCM, vertically collimated the beam. The second mirror was used to focus the beam at the experimental end-stations, and the beam size at the sample was further controlled using slits (2.4 mm horizontal × 0.4 mm vertical). The photon flux at the sample ranged from 10^{10} to 10^{12} photons s^{-1}. Incident intensities were detected by an upstream ion chamber; transmitted intensities were detected by two downstream ion chambers. Identical upstream and downstream ion chambers were 170 mm long to maximize correlation and help to normalize intensity instability. The ion chambers were operated under continuous N_2 gas flow of approximately 0.3 ± 0.1 L min^{-1} and 2.1 kV high voltage with 1 atm pressure. The electronic settings were optimized for counting statistics (Chantler *et al.*, 2000*a*,*b*).

Three standard XAS foils were placed between two downstream ion chambers and XAS was obtained at the beginning of the experiment for energy calibration. Two daisy wheels (Tran *et al.*, 2003) were placed immediately after the upstream ion chamber and immediately before the downstream ion chamber. Two rectangular apertures and one circular aperture along the daisy wheel perimeter were used to investigate the effect of scattering and fluorescence radiation. Different thicknesses of aluminium and molybdenum foils attached to the daisy wheel along the perimeter were used to characterize harmonic content of the X-ray beam (Tran *et al.*, 2003; Glover & Chantler, 2009).

Four light-tight zinc foils (*i.e.* no pinholes) 25 mm × 25 mm with thicknesses of 10 µm, 25 µm, 50 µm and 100 µm from Goodfellow were chosen such that the log attenuation of the material fall in between 0.5 and 6 over the energy range of the measurements (Nordfors, 1960; Chantler *et al.*, 2001*a*). The purity of these foils was reported as 99.95% and samples had Cd, Cu, In, Fe impurities of around 20 p.p.m. each, Pb impurities of around 100 p.p.m. and Ca, Mg, Na, Ni, Si, Sn impurities less than 10 p.p.m. The samples were mounted on a sample stage stack comprising two rotation axes and two translation axes midway between two daisy wheels (Fig. 2). The X-ray beam can be propagated through various locations of the samples by translating the sample in x and y, and alignment perpendicular to the beam is confirmed by rotation.

3. Attenuation measurements

Upstream and downstream ion chambers recorded the incident intensities (I_0) and transmission intensities (I_t), respectively, with dwell times of 1 s or 2 s. The continuous flow of N_2

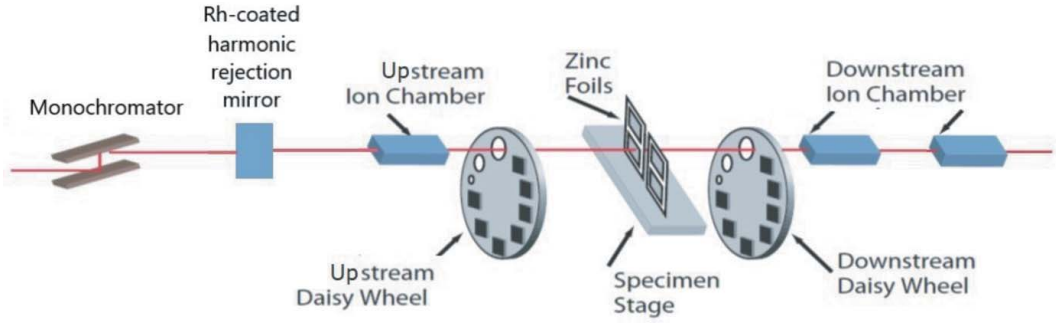

Figure 2
A schematic diagram of the experimental setup. The beamline has two mirrors – one vertical collimating mirror upstream of the DCM and one Rh-coated harmonic rejection mirror downstream of the DCM. Sample foils attached to a perspex sample holder are placed in between two daisy wheels. Ion chambers are located upstream and the downstream of the sample foils. The daisy wheels have different sized apertures, and different thickness aluminium and molybdenum foils around the perimeter to quantify the effects of scattered and fluorescent X-rays, and of the harmonic content in the incident beam, respectively. The beam direction is z, and y is the vertical direction.

gas through the ion chamber minimized the ion chamber nonlinearity caused by density fluctuations and ion gas recombination.

Using the Beer–Lambert Law (Beer, 1852; Swinehart, 1962; Fuwa & Valle, 1963), the attenuation of the beam through the sample is

$$\begin{aligned} I_t &= I_0 \exp\left(-\mu t_S\right), \\ I_t &= I_0 \exp\left\{-\left[\frac{\mu}{\rho}\right][\rho t]_S\right\}, \\ \left[\frac{\mu}{\rho}\right][\rho t]_S &= \ln\left\{\left(\frac{I_0}{I_t}\right)_S\right\}, \end{aligned} \tag{1}$$

where $[\mu/\rho]$ is the mass attenuation coefficient of the sample and $[\rho t]$ is the integrated column density of the sample. S denotes the sample.

Intensity measurements of the ion chambers at each energy point were repeated ten times to improve the signal-to-noise ratio of the readings and to measure the variance and correlation of the upstream and downstream ion chambers. Figure 3 gives the linear correlation between upstream and two downstream ion chambers for each series of ten measurements. The attenuation measurements over the energy range demonstrate a strong positive correlation between the upstream and the first downstream ion chamber resulting in a linear correlation coefficient: close to $R = 1$. The majority of the measurements in the second downstream ion chamber also indicate a strong positive linear correlation close to 1. However, the correlation coefficient of a few measurements with thick samples decreased to −0.5 at the edge energy in the second downstream ion chamber. This deviation is due to limited statistical precision for thick samples after attenuation by the first downstream ion chamber (Chantler, 2009). Low correlated data will yield increased variance and uncertainty.

The strong positive correlation of ion chamber counts dictates the method for determining the mean of the repeated intensity counts ratio of ion chambers for attenuation calculations (Chantler *et al.*, 2000*a*,*b*). Conversely, if measurements are negatively correlated, then the measurements should be analysed as the ratio of the averages rather than the preferred average of the ratios (Chantler *et al.*, 2000*a*,*b*). The uncertainty of the attenuation measurement at each energy point follows the variance and the standard error (SE) of the ten repeated measurements $[\sigma_{(I_0/I_t)_S} = \sigma_{\mathrm{SE}(I_0/I_t)_S}]$.

The X-ray beam is attenuated by the sample and by the air path between daisy wheels and the sample, ion chamber windows and ion chamber gas. The attenuation by the sample can be isolated from ion chamber differences, amplifier differences, counter differences, attenuation by the air path and windows *etc.* by normalizing using blank measurements – intensity measurements obtained from the upstream and downstream ion chambers with the absence of the samples (Chantler *et al.*, 2000*a*,*b*). These measurements normalize out all other background attenuation. Background noise and monochromator glitches also can be removed from the attenuation measurements by blank normalization in transmission. Then,

$$\left[\frac{\mu}{\rho}\right][\rho t] = \ln\left\{\frac{\overline{(I_0/I_t)_S}}{\overline{(I_0/I_t)_B}}\right\}, \tag{2}$$

where B denotes the blank measurements with uncertainty

$$\Delta\left[\frac{\mu}{\rho}\right][\rho t] = \left[\left(\frac{\sigma_{(I_0/I_t)_S}}{(I_0/I_t)_S}\right)^2 + \left(\frac{\sigma_{(I_0/I_t)_B}}{(I_0/I_t)_B}\right)^2\right]^{1/2}. \tag{3}$$

The blank normalization is one of the most significant steps in the proper measurement sequence for X-ray absorption analysis. The magnitude of mass attenuation coefficients from the 10 µm sample are scaled by from 60% to the very large 536% by the blank normalization. On correction, the uncertainty (standard deviation from variance of repeated measurements) was improved to below 1.85%. The 50 µm thickest foil data are scaled by from 12% to 97%, with uncertainties improved to below 0.13%, so clearly having significant impact even on thicker foils. The blank normalization is primarily an absolute calibration in that it affects absolute measurements and comparisons with theory moderately uniformly across the spectrum, rather than significantly

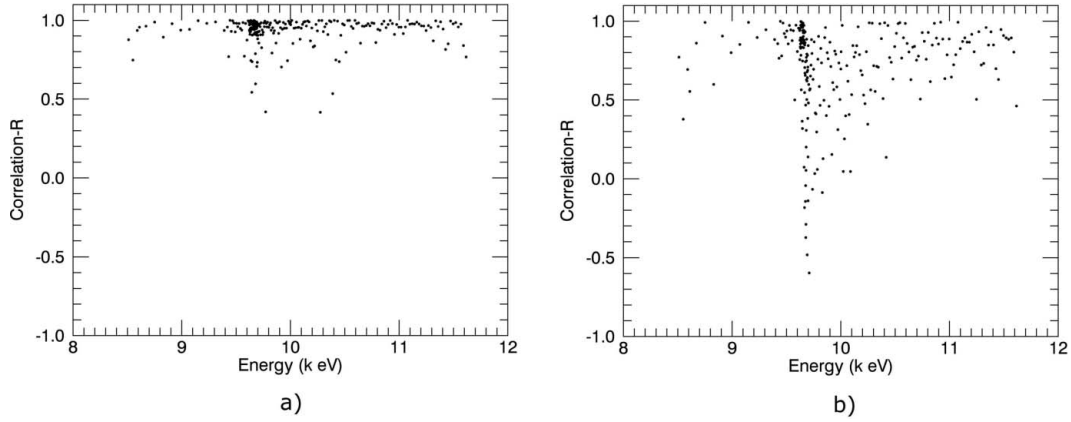

Figure 3
Linear correlation coefficient between the upstream ion chamber and (*a*) the first downstream ion chamber and (*b*) the second downstream ion chamber of 10 µm foil. Strong positive linear correlations are observed for all the measurements over all energies between the upstream ion chamber and downstream ion chambers, although a few points at the edge energy in the second downstream ion chamber have poor correlation with the upstream ion chamber.

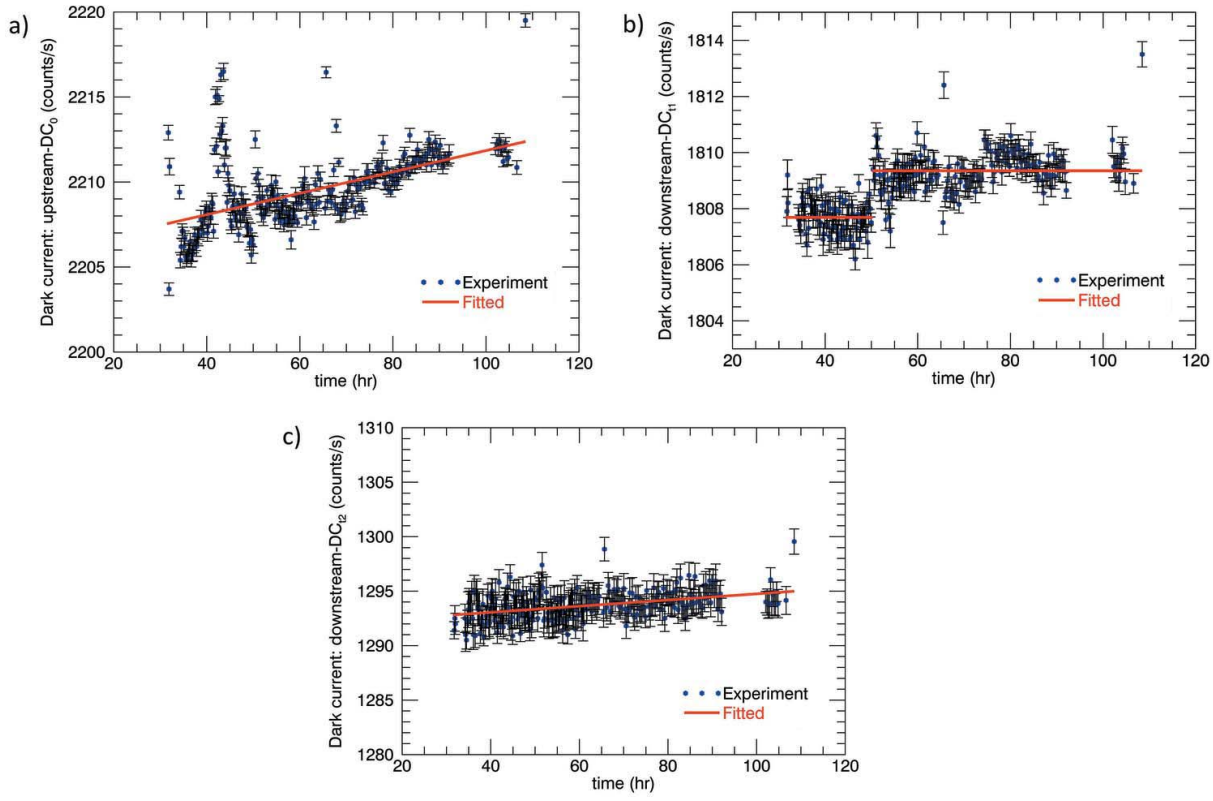

Figure 4
Dark current (DC) of (*a*) the upstream, (*b*) the first downstream and (*c*) the second downstream ion chamber versus time with uncertainties obtained from ten repetitions of measurements. A slightly increasing linear function has been fitted to the experimental measurements of the upstream ion chamber with χ_r^2 of 3. DC measurements of the first downstream ion chamber were linearly fitted with χ_r^2 of 1 across two ranges of time. DC of the second downstream ion chamber were fitted with a χ_r^2 of 1.4. Fitted data are plotted in red.

affecting detailed XAFS for example; yet for any comparison with edge jumps, theoretical coefficients and processes, it is extremely important. It also impacts upon the consistency of results in diagnosing later systematic corrections.

The readings of the ion chambers were also corrected for the dark current (DC) – intensity measurements obtained during the absence of the beam. In other words, it ensures the linearity of the detectors with respect to the Beer–Lambert law after correction for the zero offset of the detection system (Chantler *et al.*, 2012*a*).

Figure 4 gives DC measurements of the three ion chambers. A significant deviation of the upstream ion chamber data from the linear trend was observed at about 45 h due to the fluctuation of the leakage current of the ion chamber plates (Chantler *et al.*, 2000*a*). The uncertainty of the fitted line is about 2 counts s^{-1}, evaluated on the basis of the scatter in the data. The DC of the *first downstream ion chamber* [Fig. 4(*b*)] is very consistent within the first 30 to 50 h and fairly consistent in the later region. Deviations are due to back-talk from the beamline voltage variations and electronic drifts. The DC necessarily changes when the amplification range is adjusted due to saturation of high attenuation, so the DC offset will be discontinuous across these changes. The uncertainty of the DC fitting was estimated to be 1 count s^{-1} based on the scatter distribution. The DC of the *second downstream ion chamber* [Fig. 4(*c*)] is very consistent and stable with time – the percentage uncertainty of these DC measurements is higher than the other two ion chambers due to the lower offset level. Overall, almost all data fits within 1σ of the fitted trend.

Attenuation measurements are corrected by subtracting DC (the readings of the ion chambers with no beam) from the intensities of the ion chambers (with beam). Figure 5(*a*) shows the linear correlation between the ion chamber reading of the 25 µm sample foil and the DC measurements for the upstream ion chamber while Fig. 5(*b*) shows the linear correlation for the downstream ion chamber measurements. Both measurements are scattered around zero showing that the readings of the ion chambers with and without the beam are uncorrelated. Thus, the DC can be subtracted from the intensity to derive accurate measurements of attenuation. The attenuation with the DC correction is

$$\left[\frac{\mu}{\rho}\right][\rho t] = \ln\left\{\frac{\overline{\left[(I_0 - \mathrm{DC}_0)/(I_t - \mathrm{DC}_t)\right]_S}}{\overline{\left[(I_0 - \mathrm{DC}_0)/(I_t - \mathrm{DC}_t)\right]_B}}\right\}, \qquad (4)$$

where DC_0 is the DC correction for the upstream ion chamber and DC_t is the DC correction for the downstream ion chamber. The uncertainty of the intensity ratio with the DC correction is then

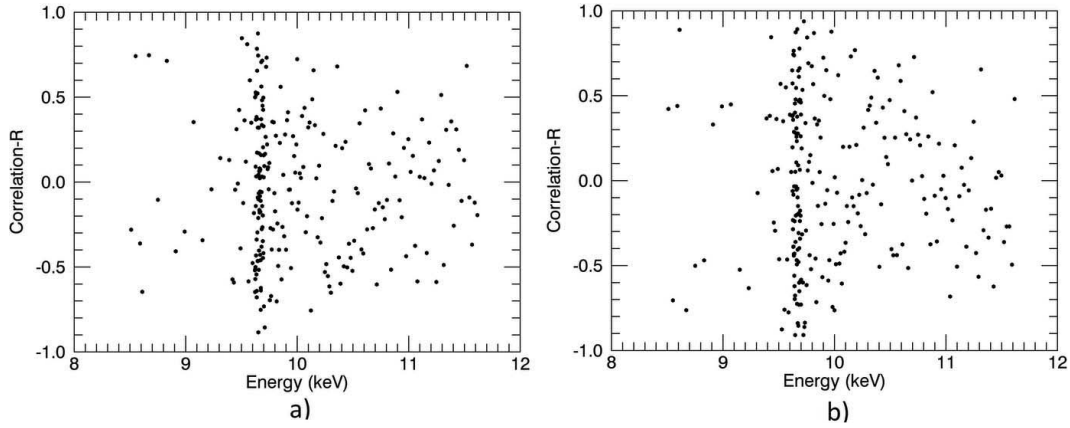

Figure 5
The linear correlation between the DC measurements and the intensities of 25 µm foil for (*a*) the upstream ion chamber and (*b*) the downstream ion chamber. Measurements are scattered around zero. Clearly, the DC and intensity measurements are uncorrelated.

$$\sigma_{\frac{(I_0-\mathrm{DC}_0)}{(I_t-\mathrm{DC}_t)}} = \left\{ \mathrm{Var}\left(\frac{I_0-\mathrm{DC}_0}{I_t-\mathrm{DC}_t}\right) + \left[\left(\frac{I_0-\mathrm{DC}_0}{I_t-\mathrm{DC}_t}\right)\frac{\sigma_{\mathrm{DC}_0}}{(I_0-\mathrm{DC}_0)}\right]^2 + \left[\left(\frac{I_0-\mathrm{DC}_0}{I_t-\mathrm{DC}_t}\right)\frac{\sigma_{\mathrm{DC}_t}}{(I_t-\mathrm{DC}_t)}\right]^2 \right\}^{1/2} \Big/ \sqrt{N}. \quad (5)$$

Figure 6 shows attenuation measurements and blank normalization for foils of different thickness before and after the DC correction. In this plot, the mass attenuation coefficients were calculated using the nominal thickness of the sample foil as specified by the supplier. The DC correction has an enormous effect on the 50 µm foil as expected. The apparent magnitudes of the mass attenuation coefficients were changed up to 57% while the uncertainty or consistency (from repeatability of measurements) was reduced significantly by up to 14.7%. The 10 µm foil has the smallest impact of the DC correction, yet it has a very significant change of up to 1.31%, affecting both structure and amplitude of the XAFS oscillations. Hence this is a major contribution to the near-edge structure, even for thin foils. A constant percentage deviation of measurements relatively to other thicknesses can be observed before and after the absorption edge. However, the attenuation was measured at the position of the beam footprint which is closest to the centre of the foil, so the thickness at the position of the beam footprint should be used to calculate the attenuation. The deviations due to this thickness effect can be diminished by calculating the absolute thickness of the centre of the foil using the full-foil mapping technique, explained below.

The X-ray beam is shut off by introducing a thick shutter in the middle of the beam path. This is supposed to be closed completely during the measurement of the dark current. There is a possibility of leaking a small amount of flux through the shutter, resulting in nonzero flux. This can weaken the DC measurements and introduce nonlinearities especially in the low-count-rate region. The transmitted X-ray beam is more attenuated for thicker foils, resulting in smaller values closer to the dark current. The effect of the incorrect DC would be more pronounced for the thicker foils as the transmitted intensities for thicker foils approach the DC values. Therefore, the DC offsets have an impact on the determination of mass

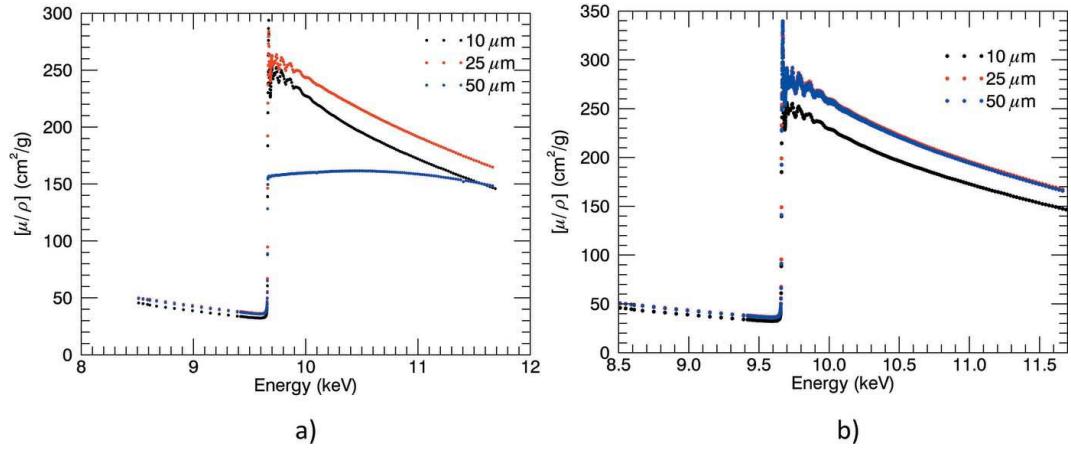

Figure 6
Attenuation of the 10 µm, 25 µm and 50 µm foils: (*a*) before and (*b*) after DC subtraction and blank normalization. Apparent scale discrepancies of attenuation after correction are particularly due to use of the nominal thickness specification by the supplier (see below).

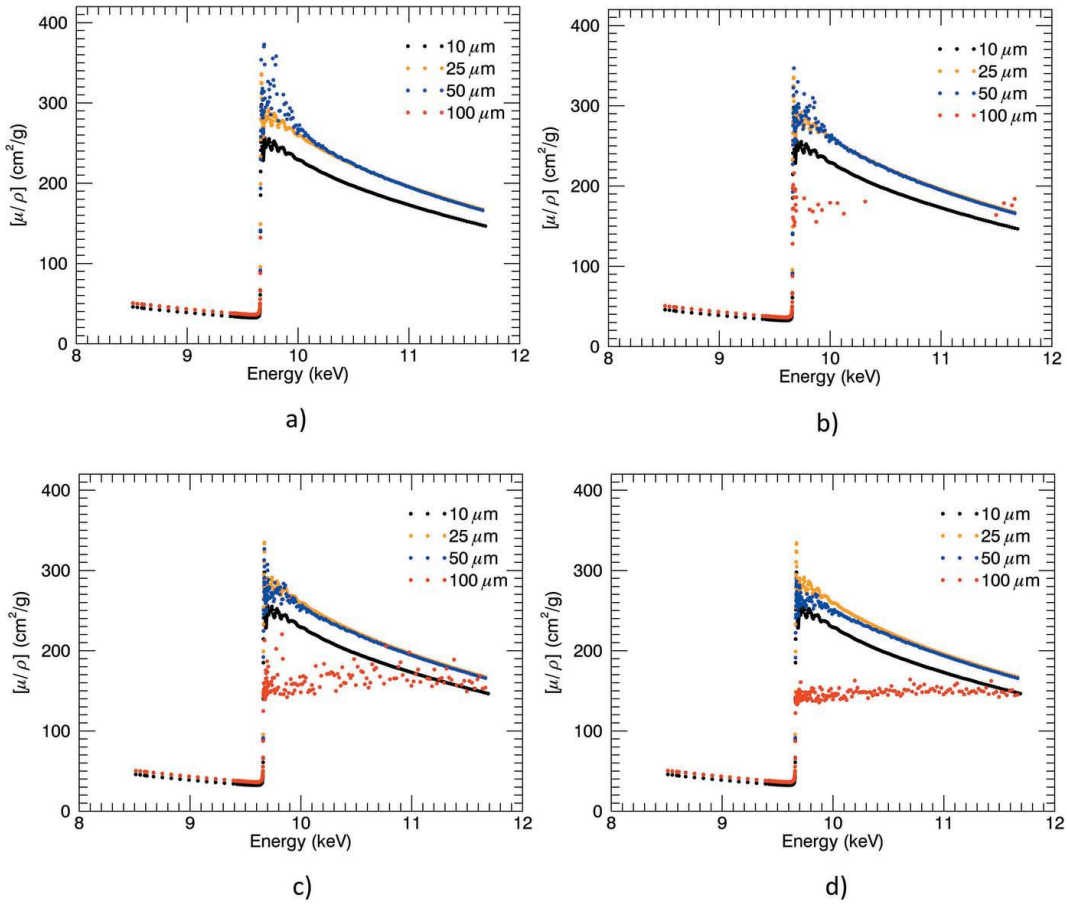

Figure 7
The mass attenuation coefficient of zinc from foils of different thickness: (*a*) without dark current offset (*i.e.* assuming the determinations of dark current are correct to within 0.5 counts); with dark current offset of (*b*) 1 counts s^{-1}, (*c*) 4 counts s^{-1} and (*d*) 6 counts s^{-1}. The oscillatory pattern above the edge was not observable for the thickest foil, confirming that the measured dark currents were accurate to within 0.5 counts.

attenuation coefficients. In the presence of any (additional) DC offset (*i.e.* an error of the measured and estimated dark current signals), the Beer–Lambert law is

$$\left[\frac{\mu}{\rho}\right][\rho t] = \ln\left\{\frac{I_0 - \mathrm{DC}_0 + \delta_{\mathrm{DC},0}}{I_\mathrm{d} - \mathrm{DC}_\mathrm{d} + \delta_{\mathrm{DC},d}}\right\}, \tag{6}$$

where δ_{DC} is an hypothesized additional DC offset. The mass attenuation coefficients with different (additional) DC offsets of 1, 4 and 6 counts s^{-1} are illustrated in Fig. 7. Clearly, determined dark current values are accurate to within 0.5 counts, especially around the edge region. The red dots indicate the thickest foil measurements, strongly attenuated above the edge. A further quantitative value of the DC offset is obtained in the harmonic systematic corrections below.

4. Full-foil mapping

The accuracy of the mass attenuation coefficient is usually limited by the inability to calculate accurate thicknesses of the sample region through which the X-ray beam passes (de Jonge *et al.*, 2006; Dachun *et al.*, 1992; Reddy *et al.*, 1976; Gerward, 1981). Full-foil mapping (de Jonge *et al.*, 2006; Islam *et al.*, 2014) and central-region mapping (Rae *et al.*, 2010*a*) are the two most accurate methodologies to calculate local integrated column densities (Tran *et al.*, 2004*a*; de Jonge *et al.*, 2007) and propagate the absolute thicknesses of the samples. The integrated column density represents the path integral of the density though the sample along the X-ray path (de Jonge *et al.*, 2004*a*). If the X-ray beam passes at (x, y, z) position though the sample, then the integrated column density is

$$[\rho t]_\mathrm{av} = \int_{-\infty}^{\infty} \rho_{xyz}\,\mathrm{d}z = \int_0^t \rho_{xyz}\,\mathrm{d}z, \tag{7}$$

where ρ_{xyz} is the mass density and t is the thickness of the sample at the (x, y) position. $[\rho t]$ is written using square brackets in order to indicate that it is a direct measurement of the product of ρ and t. It is inaccurate to measure ρ and t separately as the local density of a sample is difficult to determine and can be heterogeneous.

The mass of the sample foils m was measured using a Mettler XS205 Dual Range balance and area A was calculated using a Mitutoyo Quick Vision PRO optical coordinate measuring machine. Then, the average integrated densities over the entire area of the foils, $[\rho t]_\mathrm{av}$, were

$$[\rho t]_{\rm av} = \frac{m}{A}. \quad (8)$$

The Mettler XS205 balance had been calibrated using International Organization of Legal Metrology (IOLM) certified stainless steel calibration weights. As a consequence, the balance was stabilized and linearized to its quoted accuracy, which means it is buoyancy compensated for a density of stainless steel (8.00 g cm^{-3}). As the density of zinc is 7.1120 g cm^{-3} (Chantler, 1995, 2000), the difference must be corrected. This buoyancy correction is

$$m_{\rm true} = m_{\rm measured} + \rho_{\rm air}\, m_{\rm measured}\left(\frac{1}{\rho_{\rm zinc}} - \frac{1}{\rho_{\rm steel}}\right), \quad (9)$$

where $m_{\rm measured}$ is the measured mass and $\rho_{\rm air}$ is the density of the air. This yields a nominal correction of 20 p.p.m. for zinc metal at room temperature.

The uncertainty of mass is less than 0.025 mg and the percentage uncertainties of mass and area are about 0.011% and 0.020% or less for the sample foils. The area uncertainty is due to defects at the corner of the foils, the shadowing effect, environmental lighting effects, machine errors and eyesight (optical repeatability).

The calculated average integrated column density $[\rho t]_{\rm av}$ of 25 µm, 50 µm and 100 µm foils were then 0.018705 (6) g cm^{-2}, 0.036961 (8) g cm^{-2} and 0.07359 (2) g cm^{-2}, respectively. The calculation of mass attenuation coefficients using the average integrated column density provides a potential absolute measurement compared with the inaccuracy of using, for example, the nominal thicknesses. The use of average integrated column density contributes 0.036% or less to the percentage uncertainty of mass attenuation coefficients. The local integrated column density $[\rho t]_{\rm l}$ is then

$$[\rho t]_{\rm l} = \frac{[\mu/\rho][\rho t]_{\rm l}}{[\mu/\rho][\rho t]_{\rm av}}\,[\rho t]_{\rm av} = \frac{[\ln(I_0/I_{\rm t})]_{\rm l}}{[\ln(I_0/I_{\rm t})]_{\rm av}}\,\frac{m}{A}, \quad (10)$$

where $[\mu/\rho][\rho t]_{\rm l}$ is the attenuation at the position of the sample, where the X-ray beam passes through the sample to acquire attenuation measurements. The attenuation measurement of this local point was obtained by considering the intensity ratio. $[\mu/\rho][\rho t]_{\rm av}$ is the average attenuation over the sample surface, obtained by considering the average intensity ratio over the surface of the sample foil.

The sample foil was mounted onto a perspex sample holder along two edges to maximize the foil-only area. $[\rho t]_{\rm l}$ was obtained using the full-foil mapping method. Surface attenuation maps of four sample foils (10 µm, 25 µm, 50 µm and 100 µm foils) were obtained at energies before and after the edge energy to obtain average attenuation measurements at different energies when deriving the absolute value of mass attenuation coefficient, as measurements at various energies could be used to isolate the attenuation profiles of sample and sample holder. Attenuation maps at 8.6100 keV, 9.9991 keV and 12.9972 keV energies were obtained. The attenuation maps at higher energies emphasize the average attenuation over the surface, with less uncertainty due to the absorption edge or harmonics. Figures 8(*a*) and 8(*b*) show area maps of the 50 µm foil at 8.61 keV and at 12.9997 keV, respectively.

Conversely, the low-energy maps emphasize the sharp edges of the sample holder while the map at higher energy emphasizes the edges of the foil from the measurement The whole foil was mapped horizontally and vertically over the surface. A beam size of 2.4 mm × 0.4 mm was used to map the attenuation across the surface. The attenuation of the foil-only part was easily isolated and the attenuation at the edges was evaluated by fitting and extrapolation. The average foil attenuation follows

$$\overline{\left[\frac{\mu}{\rho}\right][\rho t]} = \frac{\sum_i p_i\% \times \ln\left[(I_0 - {\rm DC}_0)/(I_{\rm t} - {\rm DC}_{\rm t})\right]}{\sum_i p_i\%}, \quad (11)$$

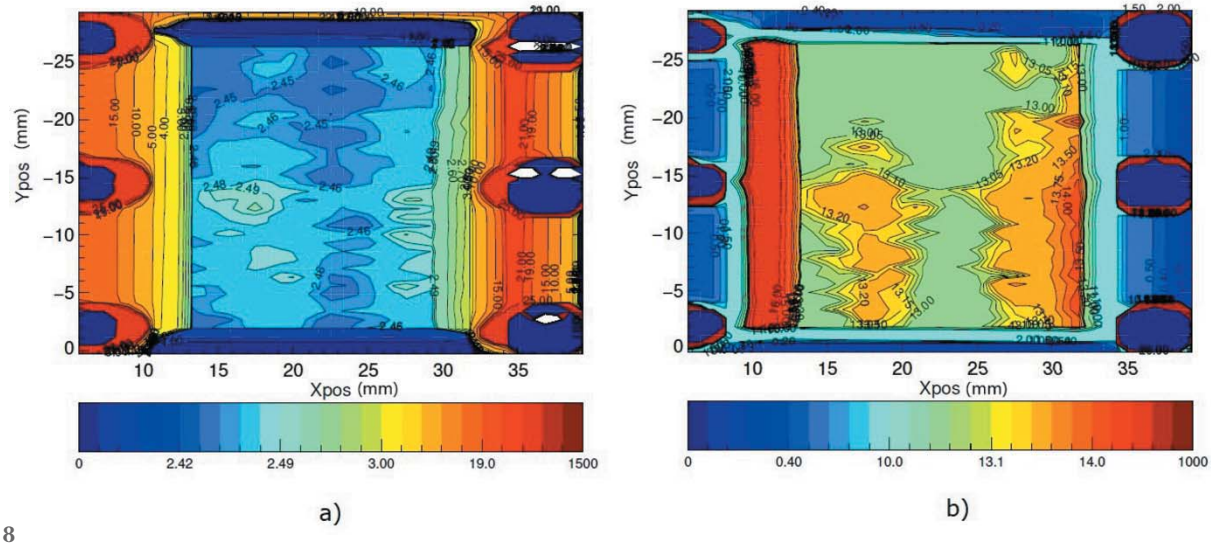

Figure 8
Attenuation maps of the 50 µm foil at (*a*) 8.61 keV and (*b*) 12.9972 keV. The low-energy map highlights the edges of the plastic holder while the higher-energy map highlights the edges of the sample foil. Circular spots indicate locations of the screws used to mount the foil. The vertical axis is $Y_{\rm pos}$.

where p_i% is the fractional percentage of the incident beam. p_i% is 100 for the foil-only area and p_i% for edges were evaluated by investigating attenuation profile of the perspex sample holder and background. The uncertainty of the attenuation measurements over the surface is

$$\sigma_{\overline{[\mu/\rho][\rho t]}} = \left(\frac{\sum_i p_i\% \times \sigma_{\ln\left(\frac{I_0 - DC_0}{I_t - DC_t}\right)}}{\sum_i p_i\%} \right)^{1/2}. \quad (12)$$

Figure 9(*a*) illustrates the attenuation measurements of the 50 µm foil, the perspex sample holder and screws. Figure 9(*b*) is the log of the attenuation and it clearly shows the attenuation variation over the foil, holder and screws. Figure 9(*c*) shows an absorption map of the foil after removing the influence of the sample holder, with a much expanded scale. The average attenuations are 1.7396 (2), 4.4274 (1) and 3.4599 (2), the mass attenuation coefficients of zinc were about 47.07 (1) cm^2 g^{-1}, 119.79 (3) cm^2 g^{-1} and 47.017 (1) cm^2 g^{-1} for the 50 µm foil at 8.61 keV and 12.997 keV and for the 100 µm foil at 8.61 keV.

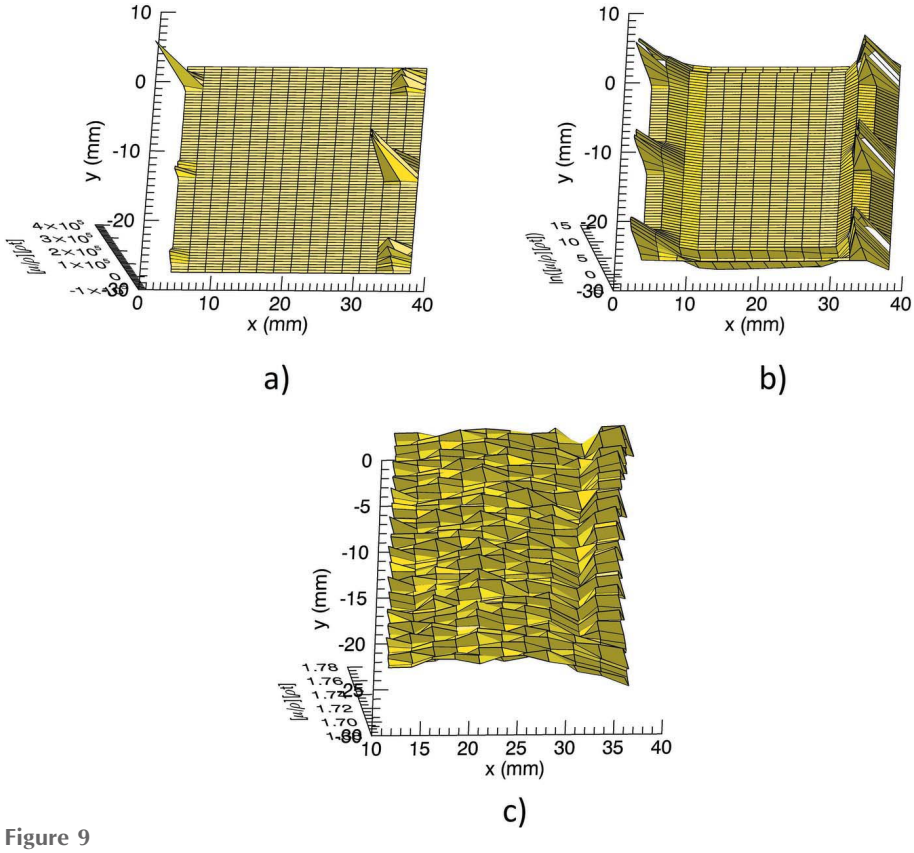

Figure 9
(*a*) The attenuation over the surface of the 50 µm foil, sample holder and screws. (*b*) Log of the attenuation over the surface of the foil, sample holder and screws; affected areas were clearly identified. (*c*) The attenuation map after removing the sample holder and screw measurements.

The local integrated column densities of 0.036783 (9) g cm^{-2} and 0.07349 (2) g cm^{-2} were derived using equation (10) for the 50 µm and 100 µm sample foils. The uncertainty associated with the local integrated column density is

$$\left[\frac{\sigma_{[\rho t]_1}}{[\rho t]_1}\right] = \left(\left[\frac{\sigma_{[\mu/\rho][\rho t]_1}}{[\mu/\rho][\rho t]_1}\right]^2 + \left[\frac{\sigma_{[\mu/\rho][\rho t]_{av}}}{[\mu/\rho][\rho t]_{av}}\right]^2 + \left[\frac{\sigma_m}{m}\right]^2 + \left[\frac{\sigma_A}{A}\right]^2 \right)^{1/2}. \quad (13)$$

5. Absolute thickness propagation

The foil thicknesses were obtained from equation (10) by dividing by the density of zinc (7.112 g cm^{-3}) (Chantler, 1995, 2000). The thicknesses of the sample foils in which the attenuation was not mapped were derived from the integrated column density of the calibrated 50 µm sample foil. The absolute thicknesses of the local point of the sample foils in the beam are 51.775 (12) µm, 103.337 (26) µm, 9.239 (2) µm and 26.124 (6) µm. The local integrated column densities were likewise corrected by the transfer of thickness scaling. Figure 10 represents the determined mass attenuation coefficients of zinc.

The apparent mass attenuation coefficients were changed compared with the supplied nominal average thicknesses, by up to 7.6% for the thinner foils, illustrating the inadequacy of using nominal thicknesses. Hence, for absolute measurements or comparison with theoretical coefficients, the careful calibration of integrated column density is extremely important. The uncertainties were improved by 0.024% for the thinnest 10 µm foil.

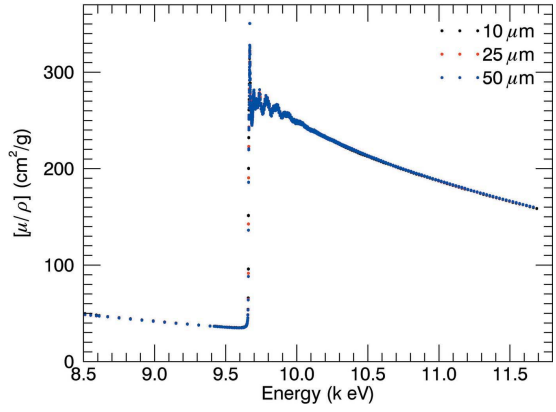

Figure 10
Mass attenuation coefficients for foils of different thickness after calculating attenuation using the local integrated density derived from the full-foil-mapping technique. Measurements are now in very good agreement and consistency; slight but significant deviations of attenuation can be observed near the edge.

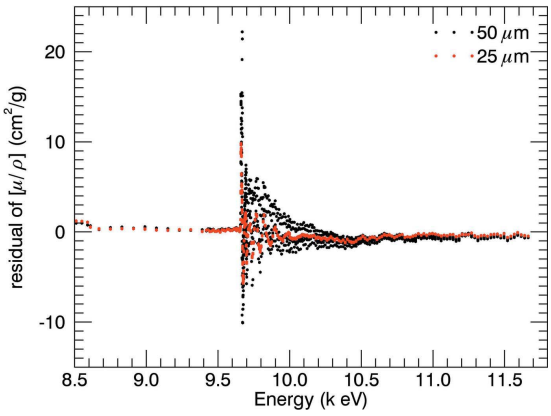

Figure 11
The discrepancy of the mass attenuation coefficients of zinc from 50 μm and 25 μm foil made with respect to the 10 μm foil measurements. This discrepancy is due to the remaining systematic effects and particularly fluorescent scattering.

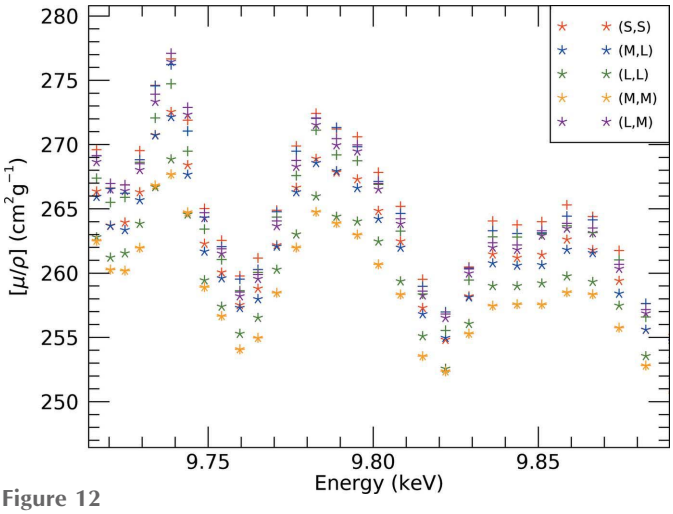

Figure 12
Discrepancy of the mass attenuation coefficients before (*) and after (+) correction for fluorescence for the 50 μm-thick sample foil. The fluorescence correction decreases the discrepancies of the mass attenuation coefficient made with different aperture combinations.

After the absolute thickness was normalized, residuals of mass attenuation coefficients of zinc from 50 μm and 25 μm foil with reference to the 10 μm foil can be seen in Fig. 11. The attenuation measurements near the absorption edge region have higher discrepancies due to remaining systematic contributions including fluorescent scattering.

6. Scattering and fluorescence

Scattering and fluorescence cause a significant systematic error of 10–20 $cm^2\ g^{-1}$ (Fig. 11). This is structural and affects the magnitude and relative significance of XAS oscillation especially in the near-edge and XAFS region. The X-ray beam incident on the sample is scattered elastically (Rayleigh) and inelastically (Compton) by the absorber or air path, with additional fluorescent radiation produced by the absorber. These three sources of scattering contribute to the ion chamber count rates and reduce the accuracy of attenuation measurements. Equation (14) gives the mass attenuation coefficient in the conventional form including the effect of elastic and inelastic scattering; and equation (15) gives the contribution of the fluorescence radiation to the measured or observed mass attenuation coefficient,

$$\left[\frac{\mu}{\rho}\right] = \left[\frac{\mu}{\rho}\right]_{\rm tot} = \left[\frac{\mu}{\rho}\right]_{\rm pe} + \left[\frac{\mu}{\rho}\right]_{\rm C} + \left[\frac{\mu}{\rho}\right]_{\rm R}, \qquad (14)$$

$$\left[\frac{\mu}{\rho}\right]_{\rm observed} = \left[\frac{\mu}{\rho}\right]_{\rm tot} - \Delta\left[\frac{\mu}{\rho}\right]_{\rm f}, \qquad (15)$$

where subscripts pe denotes the photoelectric contribution, C denotes Compton scattering, R denotes the Rayleigh scattering and f denotes the fluorescent radiation, and Δ signifies the extra radiation from fluorescence reaching the detector.

The effect of fluorescent radiation is prominent at the absorption edge and above, while Rayleigh scattering is significant at higher energies. Compton scattering could be observed below and above the absorption edge (Tran *et al.*, 2004*b*). X-ray fluorescence is isotropic. Compton scattering is mainly transverse and elastic Rayleigh scattering is primarily in the forward and backward directions. The angular dependency of the scattering can be monitored by placing apertures between the sample and the ion chambers, see Fig. 2 (Sier *et al.*, 2021).

Fluorescent scattering was observed and modelled in this experiment (Fig. 12) using different sized apertures from the upstream and downstream daisy wheels to precisely control the signature (Rae *et al.*, 2010*a*). Methods and results are discussed by Sier *et al.* (2021). A key finding was the presence of a new type a background scattering which significantly affected the data and required a new model to be developed to quantify the effect.

The mass attenuation coefficients were changed in some regions (below edge) by negligible amounts – 0.0000016% – yet by up to 35% on the rising slope of the edge, with a maximum of 6% in the near-edge region for thin foils, and by 13% or 9% for thicker foils. Variance was consequently improved in those regions.

7. Harmonic contribution

A Si(111) monochromator permits higher-order harmonics to be Bragg-diffracted as well as the intended fundamental energy. The second-order harmonic, Si(222), is forbidden. Harmonics higher than the third hamonic are negligible. Detuning of the monochromator or a harmonic suppression mirror can suppress the harmonic components of the beam. However, it is important to consider the Si(333) reflections (third-order harmonics), as the monochromation process is never perfect. The contribution of the harmonic contamination depends on the difference of the absorption at the fundamental energy and at the harmonic energy. This difference is thickness dependent. Different modalities of tuning, detuning, harmonic rejection and focusing impact upon the

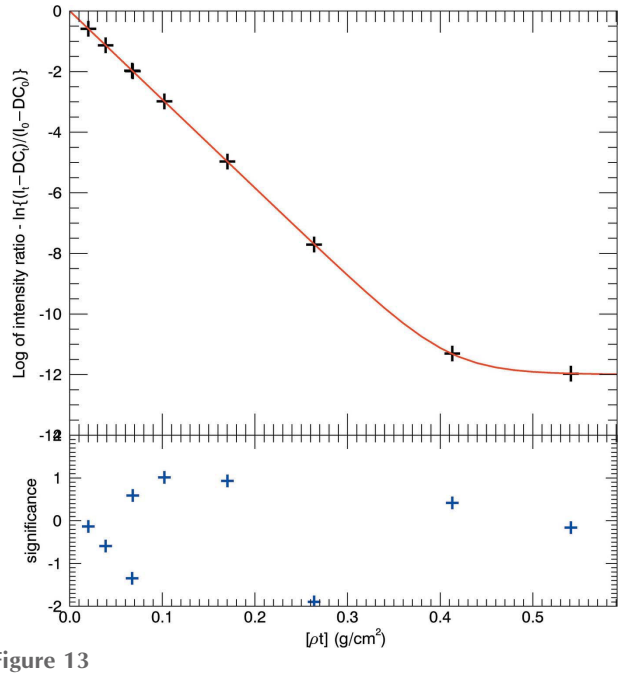

Figure 13
Harmonic contribution to the attenuation of aluminium foils at the daisy wheels for 9.7596 keV. The model equation provides a harmonic constant of 1.85×10^{-5} by fitting experimental data with a χ_r^2 of 1.66, *i.e.* almost at the limit of measurement.

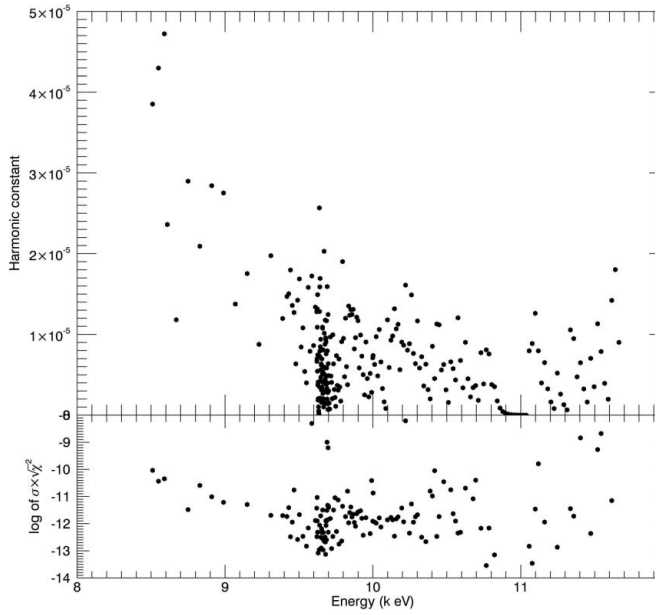

Figure 14
The effective harmonic for the X-ray beam across all energies in the experiment. The value is always less than 5×10^{-5} and lies between zero and 1×10^{-5} for most of the energies above the edge energy.

harmonic content differently at different energies, so it is generally important to quantify the effect.

Absorption can be corrected for harmonics by obtaining attenuation measurements of different thickness foil at the same mass attenuation coefficient (Tran *et al.*, 2003) (Fig. 13). If the harmonic components are present, the total transmission probability (the intensity ratio of the ion chamber counts I_t/I_0) should be the sum of the intensity ratios for each energy component. These intensity ratios are weighted by the relative intensity (effective harmonic f_n) of each component in the incident beam. f_n depends on properties of the beam, the nature of the detector and experimental geometry (Tran *et al.*, 2003; Glover & Chantler, 2009). The ion chamber efficiency has a significant impact on measuring effective harmonics. If the ion chamber detectors are insensitive to the harmonic X-rays, then this effect will be masked.

If the X-ray beam at energy E_F has a higher-order harmonic energy E_h, the intensity ratio of the ion chambers with dark current corrections is (Chantler *et al.*, 2012*a*)

$$\begin{aligned}\frac{I_t - DC_t}{I_0 - DC_0} &= \exp\left\{-\left[\frac{\mu}{\rho}\right][\rho t]\right\} \\ &= (1 - f_n)\exp\left\{-\left[\frac{\mu}{\rho}\right]_f[\rho t]\right\} \\ &\quad + f_n \exp\left\{-\left[\frac{\mu}{\rho}\right]_h[\rho t]\right\}, \end{aligned} \tag{16}$$

where f_n is the fraction of the harmonic contribution to the attenuation measurements. Attenuation of 12 different aluminium foils of thicknesses ranging from 0.1 mm to 3.8 mm were obtained. No counts were observed for the thickest foils as both fundamental and harmonic components were totally absorbed. *FFAST* tabulated mass attenuation coefficients of aluminium at fundamental energies and at harmonic energies (Chantler, 1995, 2000) were used to characterize the harmonic correction factor. The dark current offset was also included in the fitting function. The uncertainty of the attenuation measurements and the integrated column density were included in the fitting process.

The mass attenuation coefficients obtained for the aluminium foils at energy 9.7596 keV are given in Fig. 13 and fit the model well returning χ_r^2 of 1.66. The fitted harmonic content f_n was about 1.85×10^{-6} and the dark current offset was about 1×10^{-7} which confirms the measurement accuracy for the dark current to better than than 0.5 counts s^{-1} dark current offset as observed earlier. Similarly all measurements obtained at each energy point were fitted and a set of fitting parameters was obtained (Fig. 14). The percentage change of the mass attenuation coefficient with the harmonic effect obtained in this zinc experiment is up to 500 p.p.b. (for the thickest foil with the maximum correction), so this is not a major contribution to this experiment and the harmonic rejection mirror has worked well.

8. Sample roughness

Roughness of the foil deteriorates the accuracy of the attenuation calculations in absorption experiments (de Jonge *et al.*, 2007) particularly for thinner foils. Roughness is a variability in the integrated column density $[\rho t]$ and it integrates both surface and internal roughness of the sample. Integrated column density quantifies the sample matter along the X-ray beam. When an X-ray beam is incident on a rough sample, the integrated column density varies within the beam footprint and hence the mass attenuation coefficient of the

sample will be changed. The roughness is strongly dependent on the thickness and preparation of the foil (Glover *et al.*, 2009). The discrepancy of the mass attenuation coefficient $\Delta[\mu/\rho]$ due to the roughness of the sample can be modelled as

$$\Delta\left[\frac{\mu}{\rho}\right] = \frac{1}{[\rho t]_{\rm av}} \ln\left(1 - \frac{[\mu/\rho]_{\rm m}^2\, \sigma_{[\rho t]}^2}{2}\right), \qquad (17)$$

where $[\mu/\rho]_{\rm m}$ is the derived mass attenuation coefficient, $\sigma_{[\rho t]}$ is the roughness distribution parameter and $[\rho t]_{\rm av}$ is the average integrated column density of the sample.

The results of the fit, Fig. 15, yield roughness (Gaussian) distribution parameters of $\sigma_{[\rho t]} = (9.9 \times 10^{-4} \pm 4 \times 10^{-6})$ g cm^{-2} and $(9.6 \times 10^{-4} \pm 9 \times 10^{-6})$ g cm^{-2} for the 10 and 25 µm samples, respectively, relative to the smoothness of the 50 µm foil. This results in a correction of the data of up to 2.52% for the 10 µm sample and a maximum uncertainty contribution of 0.022%. The impact of this effects on the final three foil average attenuation coefficients ranges up to 1.56% at high attenuation and introduces uncertainty of up to 0.0037%. Thicknesses of 10 µm and 25 µm samples are 9.139 (2) and 26.067 (6) after normalizing data to 50 µm data along the pre-edge region where the effect of systematic error is minimum. Assuming the density of the zinc foil to be 7.1120 g cm^{-3} (Chantler, 1995, 2000), the roughness of the sample can be derived as 1.392 (6) µm for the 10 µm foil and 1.350 (13) µm for the 25 µm foil.

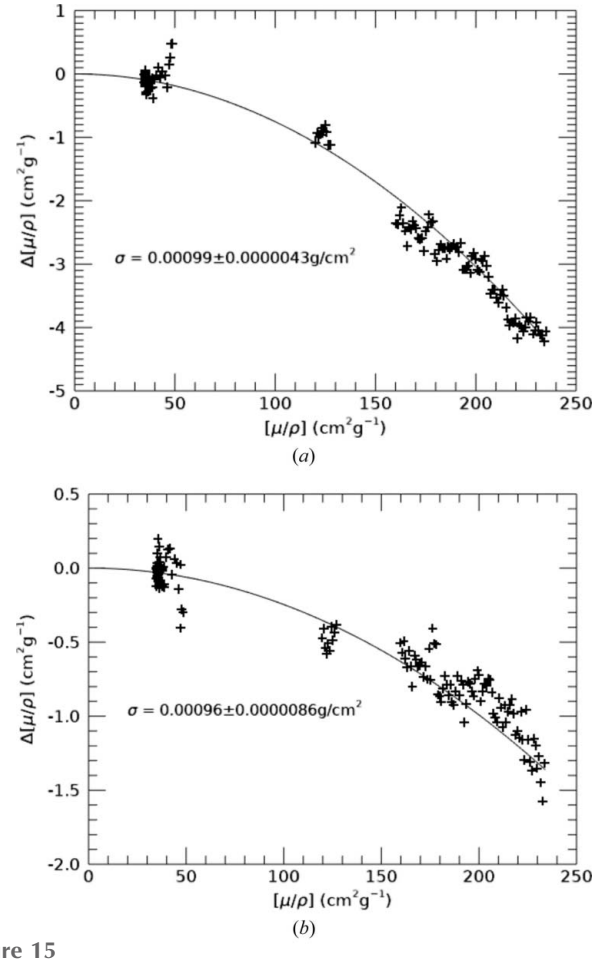

Figure 15
Fits for roughness for the (*a*) 10 and (*b*) 25 µm samples.

9. Energy bandwidth

The spectrum of energies selected by the monochromator is not an ideal delta function but in fact a narrow spectrum of energies centred upon the desired energy E_0 that is dependent on a range of parameters such as the distribution of the lattice spacing of the monochromator under thermal stress, the acceptance angle and the divergence of the incident beam. This introduces a systematic decrease in the measured attenuation coefficient (de Jonge *et al.*, 2004*b*),

$$\frac{1}{[\rho t]} \ln\left[\int_0^\infty \tilde{I}_u \exp\left[-(E - E_0)\frac{{\rm d}[\mu/\rho]_{\rm m}}{{\rm d}E}\bigg|_{E=E_0}[\rho t]\right){\rm d}E\right], \qquad (18)$$

where $\tilde{I}_u$ is the normalized incident energy profile and ${\rm d}[\mu/\rho]_{\rm m}/{\rm d}E$ is the derivative of the measured attenuation coefficient with respect to energy (Fig. 16).

We model the incident energy profile as a Gaussian distribution centred about the desired energy E_0 and extracted its full width at half-maximum by fitting it to the experimental data and found it to be $\sigma_{\rm FWHM} = 1.27$ eV with $\sigma[(\chi_r^2)(\sigma)]^{1/2} = 0.02$ eV (Fig. 17) or $\sigma_{\rm FWHM}/E_{\rm edge} \simeq 1.3 \times 101$; which is in very good agreement with the predicted value from the experimental monochromation ($\Delta E/E \simeq 1.5 \times 10^{-1}$).

The magnitude of the correction to the data due to bandwidth is significant along the absorption edge where the gradient is high, reaching up to 9.89% for the 50 µm sample with a corresponding uncertainty contribution of 0.239%. The magnitude of the correction to the final attenuation coefficients averaged across all three samples is 7.24% on the absorption edge with an uncertainty contribution of 0.033%.

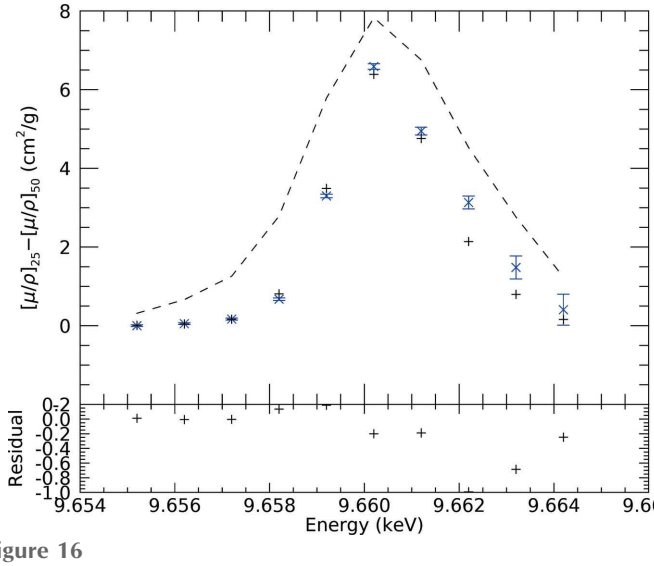

Figure 16
We see the clear presence of bandwidth, as the discrepancy in experimental data (crosses) increases with the gradient of the attenuation (dashed line) and is in good agreement with theory ($\chi_r^2 = 10.3$).

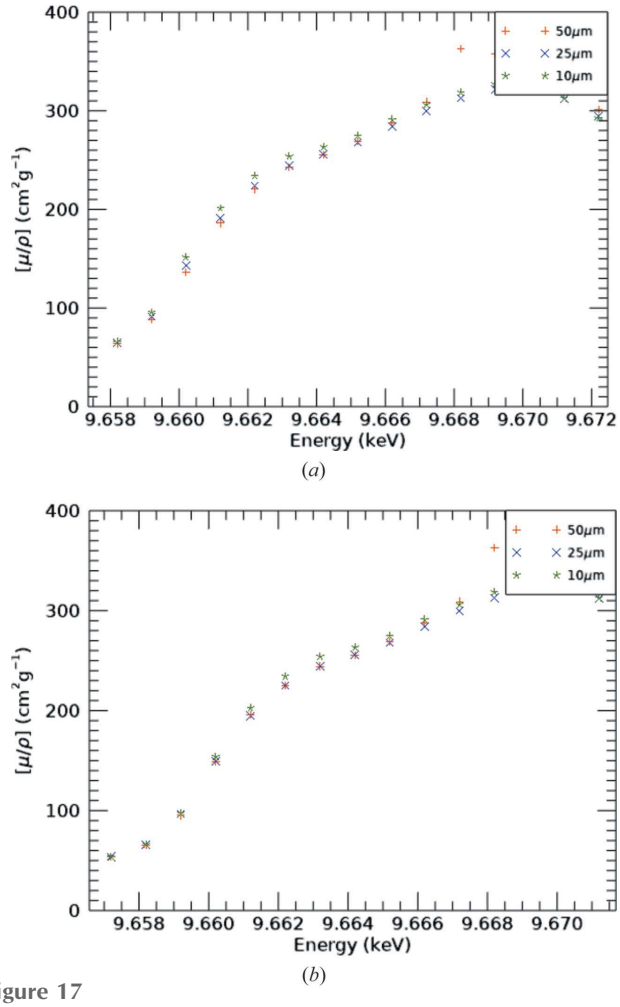

Figure 17
Plots showing the absorption edge (*a*) before and (*b*) after the correction for the effect of bandwidth. While the 10 µm data do not align perfectly with the 25 and 50 µm samples, there is still a significant improvement in the agreement between the different foils.

10. Energy measurements

The monochromator was tuned during the experiment to avoid temporal and energy instability of the monochromated energy in detuning modes on the beamline. The energy offset of the true mean energy of the beam compared with the nominal monochromator (encoder) calibration is often a functional over the hysteresis of the monochromator motor control encoder reading (Rae *et al.*, 2006). Following XERT protocols, the energy should be characterized by XRD of single crystal references or powder standards without heat load (Barnea *et al.*, 1992; Chantler *et al.*, 2001*a*, 2004; Islam *et al.*, 2014; Tantau *et al.*, 2014). However, in this experiment as the first implementation at the Australian Synchrotron, in the absence of such a calibration of energy, the standard XAFS method of using calibrated reference foils to pin the edge energy and position was used to calibrate the monochromated energies.

Often this is performed downstream of the experiment in series (*i.e.* with the sample and the reference in simultaneously to map both spectra). As seen in the fluorescence analysis, this would create a systematic error in the ion chambers used to measure the attenuation. This is not generally recommended, as it is particularly difficult to disentangle these signatures. Hence we ran separate (quick or standard XAFS) runs on the reference standards, avoiding a significant systematic error. Note the edge definition is beamline-, bandwidth-, stepsize- and resolution-dependent and affected by the pre-edge structure and Fermi levels (Chantler, 2019; Chantler *et al.*, 2020), so there remains limitations of this method to be addressed in future implementations at this beamline.

Three different standard foils of thickness 5 µm were used to obtained quick-transmission XAFS of standard foils [Fig. 18(*a*)]. The edge energy is defined as the lowest energy inflection point (the first maximum of the derivative spectrum) (Kraft *et al.*, 1996; Wong, 1999[1]): for the copper *K*-edge at 8980.476 (20) eV, the zinc *K*-edge at 9660.755 (30) eV (Kraft *et al.*, 1996) and the tantalum *L*-edge claimed to be 9881.1 eV (Wong, 1999; Burr & Bearden, 1967). The energies corresponding to the first maximum were determined by fitting the first peaks to a Gaussian curve [Fig. 18(*b*)]. Similarly, the first derivative peaks of the zinc sample foils before and after systematic corrections were also fitted.

Fitted energies of 8980.85 (12) eV, 9660.20 (10) eV and 9879.74 (20) eV were used for the copper and zinc *K*-edges and tantalum *L*-edge. The offset of the zinc *K*-edge was determined several times from the measurements obtained with different zinc sample foils and standard foil; the inflection point definition is robust; so only varies slightly with the thickness and systematics. The offset in energies from the reference to the nominal encoder-calibrated energy from the copper *K*-edge to the zinc *K*-edge is small. However, a dramatic change (1.9 eV or so) was obtained from the zinc *K*-edge to the tantalum *L*-edge which is not plausible. We conclude that the inflection point determination for tantalum is incorrect, so the calibrations at the copper and zinc *K*-edges were used to determine the energy correction. Figure 19 represents the correction against the measured energy and the uncertainty in the energy measurements.

The fitting uncertainties of the copper and zinc *K*-edges are 0.12 eV and 0.10 eV. These values are smaller than the step size 0.25 eV of the energy measurements. The uncertainties of the copper and zinc *K*-edge energy are therefore estimated to be 0.20 eV and 0.25 eV. The imputed accuracies were therefore less than 0.0038% of the beam energy.

11. Conclusion

A high-accuracy data set was collected on attenuation coefficients and XAS for zinc metal at room temperature. A five-stage sample environment was designed, constructed, controlled and successfully implemented on this beamline. Daisy wheels were successfully adapted to control systems, operated via IDL on top of EPICS. Data were collected in

[1] These results have a very fine grid giving the local structure with greater detail than most published results. These data, after scaling to give absolute results, are excellent for testing reproducibility of structure in XAFS.

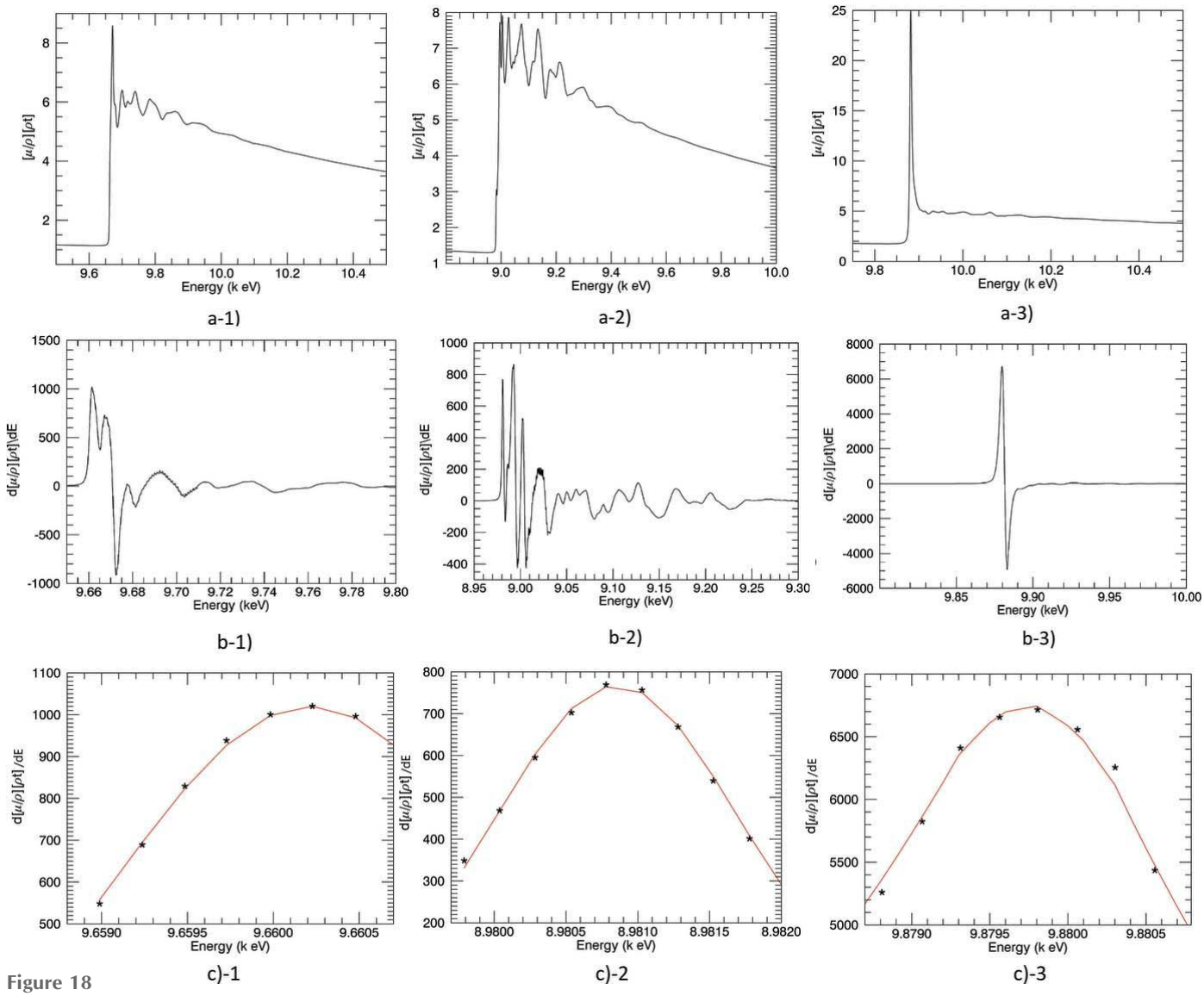

Figure 18
The X-ray absorption fine-structure spectra of (*a*-1) zinc foil, (*a*-2) copper foil and (*a*-3) tantalum foil. This procedure defined copper, zinc and tantalum edges around 8980 eV, 9660 eV and 9879 eV, respectively. The derivative spectra of X-ray absorption fine structure are presented for (*b*-1) zinc foil, (*b*-2) copper foil and (*b*-3) tantalum foil. The expanded first maxima of the derivative spectra are presented for (*c*-1) zinc, (*c*-2) copper and (*c*-3) tantalum spectra with fits (red). The edge energy is here defined by the inflection point in the first derivative following Kraft *et al.* (1996).

non-standard binary files with new data collection software written in IDL. Binary reading and confirmation of most scans was completed before the end of the run, using our readers constructed during the experiment. Protocols for monitoring and measuring dark currents, blank readings, absolute thickness, scattering, Bragg glitches and harmonics *etc.* were developed and encoded within the XERT framework across energy and throughout the data collection. The temporal cost of these, once set up and routine, is relatively modest, perhaps a factor of three for up to 100-fold improvement in accuracy.

The mode of operation was XERT-like but with energy checks rather than energy calibration and measurement. This lack of calibration points prevents any complex drift from being measured, although such drifts have been observed on several beamlines. The shifts and functional herein are relatively small and relatively stable.

Piezo tuning or detuning as a function of energy and the monitoring signal are very significant functions of energy and should be carefully monitored. Such fluctuations can lead to significant energy shift, instability and loss of signal, but are largely compensated for by the XERT methodology. There were clear Bragg monochromator glitches from three-beam diffraction in the monochromator data but also largely compensated for by the XERT normalization. Dark-current measurements show drifts and excursions by several standard deviations which would not be captured by a typical single dark-current measurement before or after the main experiment. We recommend regular dark current and blank measurements through the experiment and across the energy range. The dark current corrections change the *magnitude and structure* by from 1.31% to 57% and are significant even for thin foils. Regular use of normalization by blank measure-

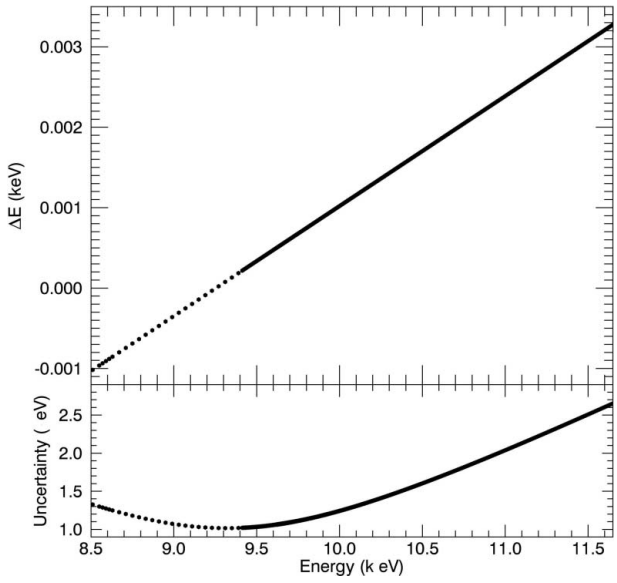

Figure 19
The correction of energy and the uncertainty versus the nominal monochromator encoder energy.

ments has a very large correction to the data of from 22% to 536% for the thinnest foil. It mainly affects the overall absorption coefficient (the absolute measurement), and theoretical parameters, with relatively little effect on the local XAFS structure. However, such absolute systematics do affect the ability of the data to reveal additional systematics which affect relative structure, XANES and XAFS like fluorescent scattering.

Tantalum standard reference foil measurements used for energy calibration have an offset or error of order 1.9 eV implying that the reference value reported in the literature is not accurate. This suggests that use of tantalum foil as a standard reference foil is imprecise and further calibration work is needed for many reference edges, possibly by using the energy calibration methodologies of XERT.

Area maps are high quality, and yield robust and accurate determinations of the absolute attenuation coefficient. For this beamline, we introduced the shutter as an automated process variable and thereby enabled a range of diagnostics to be performed remotely, on-the-fly, and regularly as part of the methodology. It enables regular and routine dark-current measurements especially for near-edge and XAFS structural and experimental amplitudes. This experiment found that no time variable was recorded in the standard or otherwise binary file data array. For this experiment, we implemented a work-around to capture the time and, by capturing log files, to diagnose time-dependent versus energy-dependent systematics. Future work will incorporate the time marker in the data files routinely, will look to incorporate energy measurement and calibration, and will explore fluorescence detection. One key challenge in this experiment was the measurement of the zinc *K*-edge region where there was also a zinc *K*-edge signal in the fluorescence background and hence in the blank measurements. It will be important moving forwards to identify and remove this contamination whether from a window or collimating aperture. Harmonics, fluorescence from the sample and background scattering and roughness are thoroughly explored and corrected for measurements in the interested energy region.

The most accurate zinc *K*-edge data sets were produced with careful investigations and corrections of significant systematic errors. These high-accuracy studies allow precise structural investigations and hence explicit explorations of solid state effects including inelastic mean free paths, inelastic and elastic scattering cross-sections, discussed in the sequel paper (Ekanayake *et al.*, 2021).

Acknowledgements

We sincerely acknowledge and are very grateful for the long and faithful collaboration with Zwi Barnea who has driven the development of XERT with us and also has driven the investigation of Zn to investigate key and long-standing anomalies in crystallography. Part of this research was undertaken on the XAS beamline at the Australian Synchrotron, part of ANSTO. We thank ANSTO and the Australian Synchrotron for their efforts and dedication to build up part of this methodology. We thank all of the synchrotron team including Jeremy Wykes, Chris Glover and Susan Cumberland. We thank our attending team members Stephen P. Best and Victor A. Streltsov for their contributions here and in earlier experiments. We thank Hamish A Melia for his support for this work and Ryan J. Trevorah and Geoffrey P. Cousland for helpful reading of the manuscript.

References

Al-Buriahi, M. S. & Tonguc, B. T. (2020). *Radiat. Phys. Chem.* **166**, 108507.
Barnea, Z., Creagh, D. C., Davis, T. J., Garrett, R. F., Janky, S., Stevenson, A. W. & Wilkins, S. W. (1992). *Rev. Sci. Instrum.* **63**, 1069–1072.
Beer, A. (1852). *Ann. Phys. Chem.* **162**, 78–88.
Berger, M. J. & Hubbell, J. H. (1987). *XCOM: Photon Cross Sections on A National Bureau of Standards.* Technical Report NBSIR-87-3597. Center for Radiation, National Bureau of Standards, Washington, DC, USA.
Borges, J. A. R., Pires, L. F. & Costa, J. C. (2014). *Sci. World J.* **2014**, 584871.
Burr, F. & Bearden, J. A. (1967). *Rev. Mod. Phys.* **39**, 125–142.
Chantler, C. T. (1995). *J. Phys. Chem. Ref. Data*, **24**, 71–643.
Chantler, C. T. (2000). *J. Phys. Chem. Ref. Data*, **29**, 597–1056.
Chantler, C. T. (2009). *Eur. Phys. J. Spec. Top.* **169**, 147–153.
Chantler, C. T. (2019). *A little dictionary of Crystallography [IUCR Commission on Crystallographic Nomenclature]*, edited by A. Authier and G. Chapuis, p. 286 Dordrecht: Kluwer Academic Publishers.
Chantler, C. T., Barnea, Z., Tran, C. Q., Rae, N. A. & de Jonge, M. D. (2012*a*). *J. Synchrotron Rad.* **19**, 851–862.
Chantler, C. T., Rae, N. A., Islam, M. T., Best, S. P., Yeo, J., Smale, L. F., Hester, J., Mohammadi, N. & Wang, F. (2012*b*). *J. Synchrotron Rad.* **19**, 145–158.
Chantler, C. T., Smale, L. F. & Hudson, L. T. (2020). *International Tables for Crystallography*, Vol. C, edited by T. R. Welberry, ch 4.2.2. Dordrecht: Kluwer Academic Publishers.
Chantler, C. T., Tran, C. Q., Barnea, Z., Paterson, D., Cookson, D. J. & Balaic, D. X. (2001*a*). *Phys. Rev. A*, **64**, 062506.

Chantler, C. T., Tran, C. Q. & Cookson, D. J. (2004). *Phys. Rev. A*, **69**, 042101.
Chantler, C. T., Tran, C. Q., Paterson, D., Barnea, Z. & Cookson, D. J. (2000*a*). *X-ray Spectrom.* **29**, 449–458.
Chantler, C. T., Tran, C. Q., Paterson, D., Barnea, Z. & Cookson, D. J. (2001*b*). *Radiat. Phys. Chem.* **61**, 347–350.
Chantler, C. T., Tran, C. Q., Paterson, D., Cookson, D. J. & Barnea, Z. (2000*b*). *X-ray Spectrom.* **29**, 459–466.
Creagh, D. C. (1976). *J. Phys. E: Sci. Instrum.* **9**, 88–90.
Creagh, D. C. & Hubbell, J. (1999). *International Tables for Crystallography*, 2nd ed, Vol. C, edited by E. Prince, Section 4.2.4. Wiley.
Dachun, W., Xunliang, D., Xinfu, W., Hua, Y., Hongyu, Z., Xinyin, S. & Guanghua, Z. (1992). *Nucl. Instrum. Methods Phys. Res. B*, **71**, 241–248.
Ekanayake, R. S. K., Chantler, C. T., Sier, D., Schalken, M. J., Illig, A. J., de Jonge, M. D., Johannesen, B., Kappen, P. & Tran, C. Q. (2021). *J. Synchrotron Rad.* **28**, 000–000. [RV5147].
Fuwa, K. & Valle, B. L. (1963). *Anal. Chem.* **35**, 942–946.
Gerward, L. (1981). *J. Phys. B: At. Mol. Phys.* **14**, 3389–3395.
Glover, J. L. & Chantler, C. T. (2009). *X-ray Spectrom.* **38**, 510–512.
Glover, J. L., Chantler, C. T., Barnea, Z., Rae, N. A. & Tran, C. Q. (2010). *J. Phys. B At. Mol. Opt. Phys.* **43**, 085001.
Glover, J. L., Chantler, C. T. & de Jonge, M. D. (2009). *Phys. Lett. A*, **373**, 1177–1180.
Henke, B. L., Lee, P., Tanaka, T. J., Shimabukuro, R. L. & Fujikawa, B. K. (1982). *At. Data Nucl. Data Tables*, **27**, 1–144.
Hopkins, J. I. (1959). *J. Appl. Phys.* **30**, 185–187.
Huang, H. K. & Wu, S. C. (1976). *Comput. Biol. Med.* **6**, 337–343.
Islam, M. T., Rae, N. A., Glover, J. L., Barnea, Z., de Jonge, M. D., Tran, C. Q., Wang, J. & Chantler, C. T. (2010). *Phys. Rev. A*, **81**, 022903.
Islam, M. T., Tantau, L. J., Rae, N. A., Barnea, Z., Tran, C. Q. & Chantler, C. T. (2014). *J. Synchrotron Rad.* **21**, 413–423.
Jonge, M. D., Barnea, Z., Tran, C. Q. & Chantler, C. T. (2004*a*). *Meas. Sci. Technol.* **15**, 1811–1822.
Jonge, M. D. de, Tran, C. Q., Chantler, C. T. & Barnea, Z. (2006). *Opt. Eng.* **45**, 046501.
Jonge, M. D. de, Barnea, Z., Tran, C. Q. & Chantler, C. T. (2004). *Phys. Rev. A*, **69**, 022717.
Jonge, M. D. de, Tran, C. Q., Chantler, C. T., Barnea, Z., Dhal, B. B., Paterson, D., Kanter, E. P., Southworth, S. H., Young, L., Beno, M. A., Linton, J. A. & Jennings, G. (2007). *Phys. Rev. A*, **75**, 032702.
Kaur, K., Gupta, R., Saraf, S. A. & Saraf, S. K. (2014). *Compr. Rev. Food. Sci. Food. Saf.* **13**, 358–376.
Kraft, S., Stümpel, J., Becker, P. & Kuetgens, U. (1996). *Rev. Sci. Instrum.* **67**, 681–687.
Ménesguen, Y., Gerlach, M., Pollakowski, B., Unterumsberger, R., Haschke, M., Beckhoff, B. & Lépy, M. (2016). *Metrologia*, **53**, 7–17.
Nordfors, B. (1960). *Ark. Fys.* pp. 1–2.
Parratt, L. G., Porteus, J. O., Schnopper, H. W. & Watanabe, T. (1959). *Rev. Sci. Instrum.* **30**, 344–347.
Rae, N. A., Chantler, C. T., Barnea, Z., de Jonge, M. D., Tran, C. Q. & Hester, J. R. (2010*a*). *Phys. Rev. A*, **81**, 022904.
Rae, N. A., Chantler, C. T., Tran, C. Q. & Barnea, Z. (2006). *Radiat. Phys. Chem.* **75**, 2063–2066.
Rae, N. A., Glover, J. L. & Chantler, C. T. (2010*b*). *Nucl. Instrum. Methods Phys. Res. A*, **619**, 47–50.
Rae, N. A., Islam, M. T., Chantler, C. T. & de Jonge, M. D. (2010*c*). *Nucl. Instrum. Methods Phys. Res. A*, **619**, 147–149.
Reddy, D. K. S., Premachand, K., Murty, V. R. K., Rao, J. R. & Lakshminarayana, T. (1976). *Phys. Rev. A*, **13**, 326–329.
Sier, D., Ekanayake, R. S. K. & Chantler, C. T. (2021). *Acta Cryst.* Submitted.
Swinehart, D. F. (1962). *J. Chem. Educ.* **39**, 333–335.
Tantau, L. J., Chantler, C. T., Bourke, J. D., Islam, M. T., Payne, A. T., Rae, N. A. & Tran, C. Q. (2015). *J. Phys. Condens. Matter*, **27**, 266301.
Tantau, L. J., Islam, M. T., Payne, A. T., Tran, C. Q., Cheah, M. H., Best, S. P. & Chantler, C. T. (2014). *Radiat. Phys. Chem.* **95**, 73–77.
Tran, C. Q., Barnea, Z., de Jonge, M. D., Dhal, B. B., Paterson, D., Cookson, D. J. & Chantler, C. T. (2003). *X-ray Spectrom.* **32**, 69–74.
Tran, C. Q., Chantler, C. T., Barnea, Z. & de Jonge, M. D. (2004*a*). *Rev. Sci. Instrum.* **75**, 2943–2949.
Tran, C. Q., Chantler, C. T., Barnea, Z., Jonge, M. D., Dhal, B. B., Chung, C. T., Paterson, D. & Wang, J. (2005). *J. Phys. B At. Mol. Opt. Phys.* **38**, 89–107.
Tran, C. Q., Jonge, M. D., Barnea, Z. & Chantler, C. T. (2004*b*). *J. Phys. B At. Mol. Opt. Phys.* **37**, 3163–3176.
Unonius, L. & Suortti, P. (1989). *J. Appl. Cryst.* **22**, 46–52.
Wong, J. (1999). *Reference X-ray Spectra of Metal Foils.* EXAFS Materials, Inc., 871 El Cerro Blvd, Danville, CA, USA.